ADVANCED FUNCTIONAL MATERIALS

Supporting Information

for *Adv. Funct. Mater.*, DOI: 10.1002/adfm.201705588

Sol–Gel Synthesis of Robust Metal–Organic Frameworks for Nanoparticle Encapsulation

Joshua P. Mehta, Tian Tian, Zhixin Zeng, Giorgio Divitini, Bethany M. Connolly, Paul A. Midgley, Jin-Chong Tan, David Fairen-Jimenez, and Andrew E. H. Wheatley**

Supporting Information

Sol-Gel Synthesis of Robust Metal-Organic Frameworks for Nanoparticle Encapsulation

Joshua. P. Mehta, Tian Tian, Zhixin Zeng, Giorgio Divitini, Bethany M. Connolly, Paul A. Midgley, Jin-Chong Tan, David Fairen-Jimenez and Andrew E. H. Wheatley**

Table of Contents

1. Characterization of materials

$Zn(NO_3)_2 \cdot 6H_2O$ (98%) and 2-methylimidazole (97%) were purchased from Alfa Aesar; ethanol (≥99.5%), $SnCl_4 \cdot 5H_2O$ and methylene blue were purchased from Sigma-Aldrich; NaOH pellets (≥97%) were purchased from Fischer Scientific. Chemicals were used as received, without further purification. $SnO_2@_{mono}$ZIF-8 was characterised utilising: focused ion beam-X-ray photoelectron spectroscopy (FIB-XPS), focused ion beam-scanning electron microscopy (FIB-SEM), transmission electron microscopy (TEM), scanning transmission electron microscopy-energy dispersive X-ray spectroscopy (STEM-EDX), thermogravimetric analysis (TGA), powder X-ray diffraction (PXRD), N_2 adsorption isotherms at 77 K, mercury porosimetry, nanoindentation studies, attenuated total reflectance FT infrared spectroscopy (FT-IR), inductively coupled plasma-optical emission spectroscopy (ICP-OES) and elemental analysis (EA) techniques. Photocatalytic properties were explored by monitoring the degradation of model organic volatile methylene blue (MB) under simulated solar irradiation produced by a 150 W xenon lamp fitted with an air mass 1.5 global (AM 1.5G) filter (Solar Simulator model LSO106, 1 sun illumination, 100 mW cm^{-2}). The degradation of aqueous MB (25 mL, 1.55×10^{-5} M, pH 7.30) was recorded by monitoring the reduction in λ_{max} at 664 nm using a BOECO S-22 and a Perkin Elmer Lambda 750 UV/vis/NIR spectrometer for single and multi-wavelength measurements, respectively. An ice-cold water bath prevented dye evaporation under impeding light and thermal dye degradation. Control experiments were run (i) without irradiation in the presence of $SnO_2@_{mono}$ZIF-8 and (ii) with irradiation in the absence of composite. Low loading experiments used 0.4 g of composite, whilst high loading sets used 1.7 g. Composite was collected under gravity filtration and dried under ambient conditions overnight before recycling. Each cycle under solar irradiation was performed parallel to a control in the dark, administering the same recycling procedure. All experiments were triplicated. Hydroxyl radicals produced during photocatalysis were detected using a terephthalic acid probe.

PXRD patterns were measured on a PANalytical Empyrean diffractometer fitted with an X'celerator detector and using a Cu-Kα_1 (λ = 1.5406 Å) source with a step size of 0.002° and a scanning speed of 0.022° s^{-1} at 40 kV and 40 mA. SEM images were obtained on a FEI Helios Nanolab with an accelerating voltage of 5 keV. TEM images were collected on a FEI Tecnai G2 and a FEI Osiris S/TEM operated in scanning mode with an accelerating voltage of 200 keV. For the TEM images of the mother liquor, a 1 mL sample of the reaction medium

was withdrawn after 15 minutes and diluted 10 times in ethanol. 25 μL of the resulting solution was drop-coated onto a copper grid and the ethanol evaporated at room temperature. For high angle annular dark field (HAADF) images and EDX analysis the monolithic sample was pressed into a copper grid, with the EDX signal collected using a set of Bruker Super-X detectors. Thermogravimetric analyses were performed on a TA Instruments TGA 500, ranging from room temperature to 750 °C in nitrogen, using a ramp rate of 10 °C min^{-1}. N_2 adsorption isotherms were obtained at 77 K using a Micrometrics 3 Flex instrument. All samples were degassed in situ at 110 °C for 6 hours before measurement. The recycled $SnO_2@_{mono}$ZIF-8 samples were not washed after photocatalysis. Mercury porosimetry data was obtained using an AutoPore IV 9500 instrument employing pressures up to 2000 bar. An Exeter analytical CE 440 elemental analyser at a combustion temperature of 975 °C was utilised for C, H, and N analysis whilst Zn and Sn analysis was performed on a Thermo Scientific iCAP 7400 ICP-OES analyser against 1 ppm and 10 ppm standards. $SnO_2@_{mono}$ZIF-8 was filtered, soaked in deionised water, and dried under conventional and vacuum oven environments before elemental analyses were performed again. FIB-XPS measurements were obtained using a Thermo Scientific K-Alpha system. The binding energy was calibrated internally based on the C(1s) line position. Each etch was conducted at full power (ion energy = 3000 eV, current = 'high') for 20 seconds. The estimated sputter rate of the Ta_2O_5 source was 0.68 nm sec^{-1}, leading to an estimated total etching depth of 122 nm, whilst the diameter of the area analysed was 400 μm. FT-IR spectra were collected on a Thermo Scientific Nicolet iS50 FT-IR spectrometer in ATR mode. Nanoindentation measurements were performed using an MTS Nano Indenter XP system equipped with a Berkovich diamond tip. The continuous stiffness method was employed and epoxy mounted monolithic samples were indented up to a maximum surface penetration depth of 2000 nm, in accordance with the established methodology for characterizing MOFs,[1] taking Poisson's ratio of 0.33[2] to determine the upper bounds of Young's modulus, *E*. In photocatalytic experiments, 3 mL aliquots taken at 15-minute intervals over three hours gave the concentration of dye as a function of time. Each aliquot was returned to the original dye solution immediately after analysis. Hydroxyl radicals ($OH^{\bullet}$) produced during photocatalysis were detected by dispersing 0.4 g of $SnO_2@_{mono}$ZIF-8 in a basic aqueous solution of terephthalic acid (TA) (10^{-4} M). The solution was exposed to simulated solar irradiation and the maximum fluorescence emission intensity of 2-hydroxyterephthalic acid measured after excitation at 315 nm.

2. SnO_2 analysis

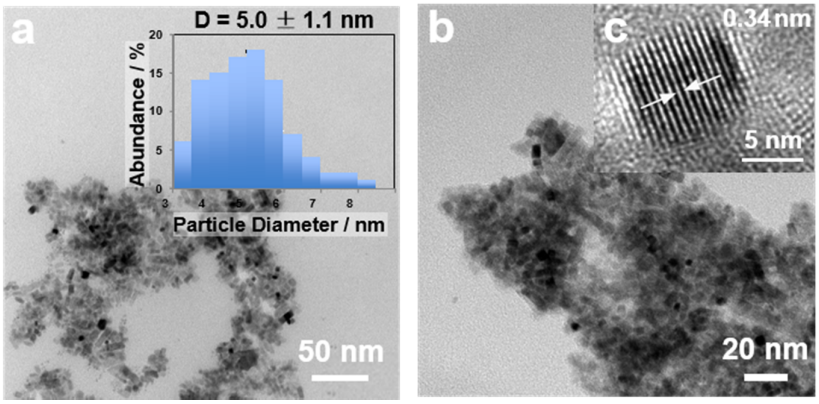

Figure S1. Representative bright field TEM (Scale bars 50 nm (a) and 20 nm (b)) and HRTEM ((c), scale bar 5 nm) micrographs of SnO_2 nanoparticles alongside particle size distribution ((a), inset). Error is the standard deviation over 100 values of particle diameters.

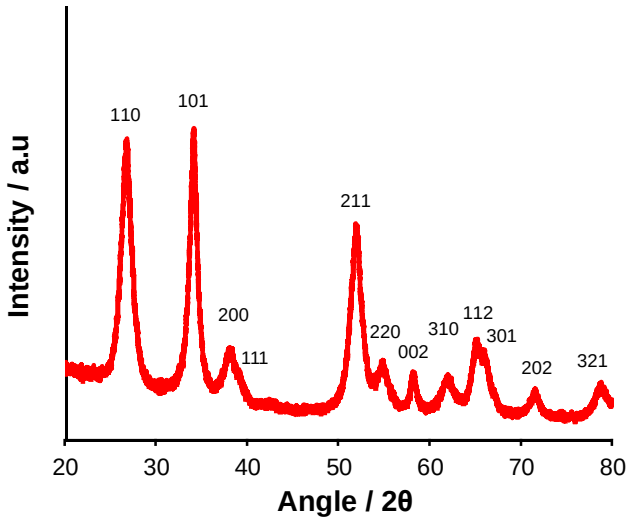

Figure S2. Indexed X-ray powder diffraction pattern of SnO_2 nanoparticles prepared in this work.

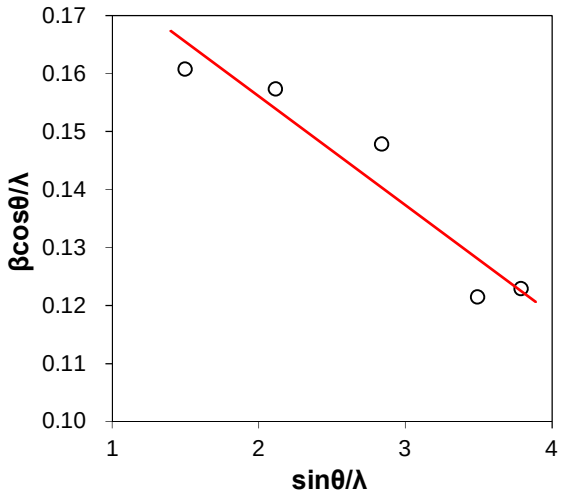

Figure S3. Williamson-Hall plot of $\frac{\beta cos\theta}{\lambda}$ against $\frac{sin\theta}{\lambda}$ for SnO_2 nanoparticles prepared in this work.

The diffraction pattern (Figure S2) was analyzed using the Scherrer (Equation S1) and Williamson-Hall (Equation S2) equations to give estimates of particle size by accounting for size and strain broadening.

$$D = \frac{K\lambda}{\beta cos\theta} \qquad \text{(Equation S1)}$$

$$\beta cos\theta = \frac{k\lambda}{D} + \eta sin\theta \qquad \text{(Equation S2)}$$

where D is the mean crystallite size, β is the full-width-at-half-maximum (FWHM) in radians, θ is the angle in degrees, λ is the wavelength of incident radiation (1.5406 Å for the Cu-Kα_1 source), η is the strain in the crystallite lattice, K is the dimensionless shape factor and k is a constant, typically close to unity.[3]

The (110), (211), (112), (202) and (200) peaks were utilized in the Williamson-Hall analysis (Equation S2), assuming a constant of unity. $\frac{\beta cos\theta}{\lambda}$ was plotted against $\frac{sin\theta}{\lambda}$ to give an intercept of $\frac{1}{D}$ and gradient η, which were used to determine crystallite size and lattice strain respectively.

Peak broadening in the PXRD pattern indicated small particle size, with the Scherrer formula (Equation S1) giving an average crystallite size of 5.03 nm, assuming a dimensionless shape factor of 0.89 (Figure S2). It is important to note that this gives a lower limit for particle size. The value is in close agreement with results obtained from the

Williamson-Hall plot,[4] which gives an average crystallite size of 5.17 nm and a strain of -0.0188 (Figure S3). This negative strain value indicates a compressive lattice strain in the nanoparticles. Diffraction peaks were indexed to the tetragonal crystal structure known to be associated with SnO_2 using the (200) and (002) peaks, producing lattice parameters, a = 4.729 Å and c = 3.172 Å, in good agreement with reported values (JCPDS card no. 41-1445).

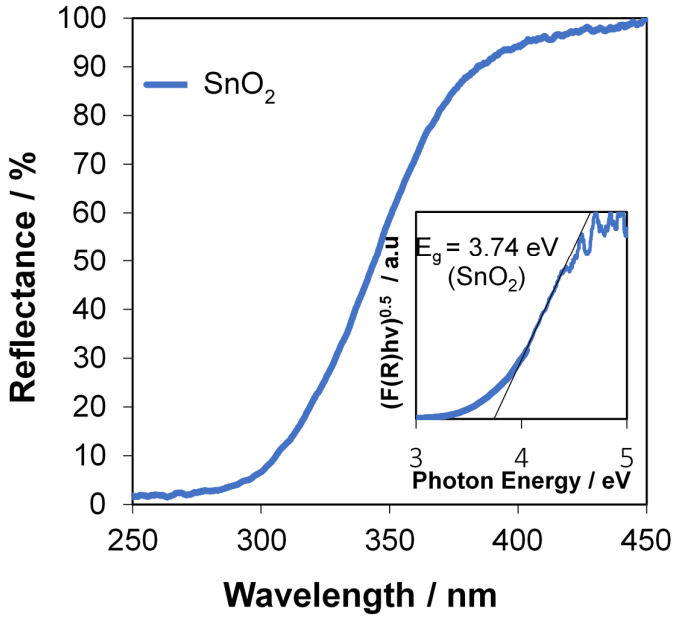

Figure S4. Solid state UV-vis spectrum and Tauc plot (inset) of SnO_2 NPs synthesized in this work. The Kubelka-Munk function, F(R), is estimated using: $F(R) = \frac{(1-R)^2}{2R}$ where R denotes the reflectance.

3. SnO_2@$_{mono}$ZIF-8 analysis

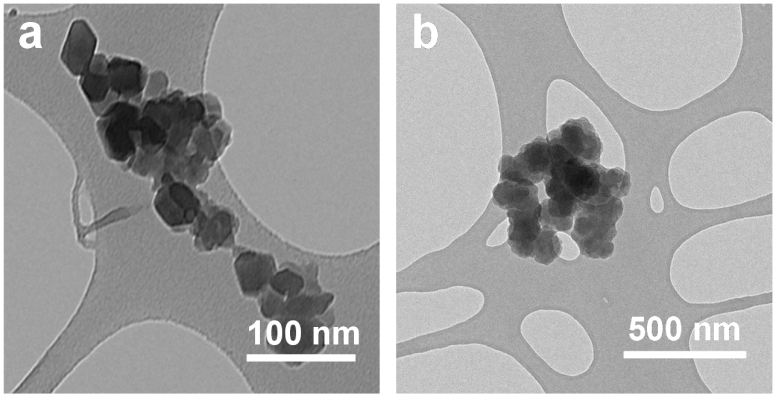

Figure S5. Representative TEM micrographs of the mother liquors associated with the preparation of $_{mono}$ZIF-8 (a) and SnO_2@$_{mono}$ZIF-8 (b) taken at 15 minutes reaction time.

Table S1. Chemical microanalyses of $_{mono}$ZIF-8 (simulated and experimental) and fresh SnO_2@$_{mono}$ZIF-8 based on nitrogen and tin contributions acquired from elemental analysis and ICP-OES data. Errors are the standard deviation in triplicated Sn and N wt% values with zero readings occurring due to numerical rounding. Deviation from 100 % total loading is attributed to residual reagents and solvents trapped in the materials.

Materials	Composition Wt.%						
	C	H	N	Sn	Zn	SnO_2	ZIF-8
Sim. ZIF-8	42.2	4.4	24.6	-	28.7	-	100
Exp. $_{mono}$ZIF-8	41.7±0.0	4.5±0.0	24.4±0.3	-	26.2±0.4	-	99.0±1.1
SnO_2@$_{mono}$ZIF-8	40.5±0.4	4.6±0.1	23.1±0.3	1.6±0.1	24.5±0.4	2.0±0.1	93.9±1.2
SnO_2@$_{mono}$ZIF-8 (1 cycle)	39.3±0.4	4.3±0.1	23.5±0.3	2.6±0.1	24.5±0.4	3.3±0.1	95.4±1.2
SnO_2@$_{mono}$ZIF-8 (5 cycles)	39.1±0.4	4.2±0.1	23.2±0.3	2.2±0.1	25.2±0.4	2.8±0.1	94.4±1.2
SnO_2@$_{mono}$ZIF-8 (10 cycles)	36.7±0.4	3.95±0.1	21.6±0.3	4.1±0.1	25.9±0.4	5.2±0.1	87.8±1.2

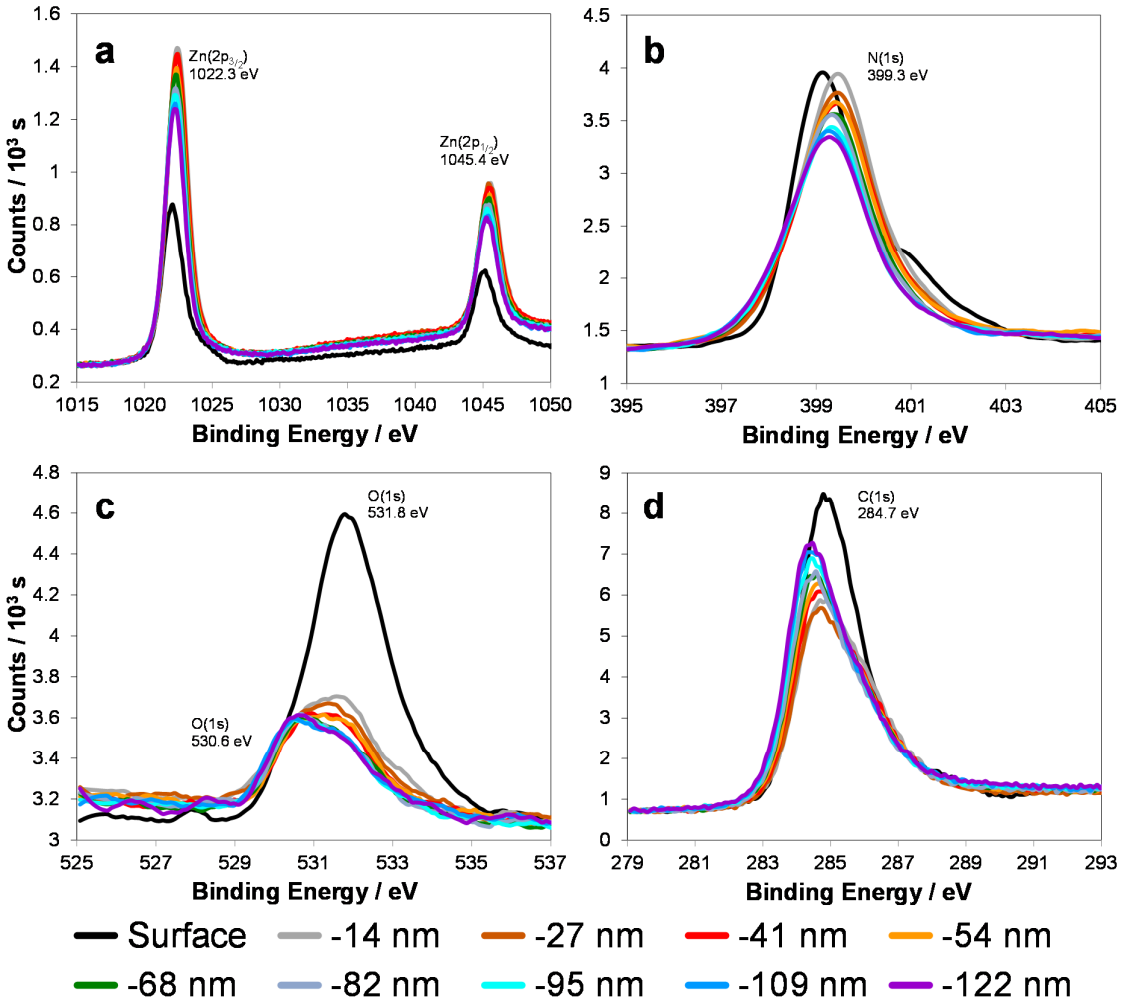

Figure S6. Selected FIB-XPS data for Zn (a), N (b), O (c) and C (d) for etched layers of SnO_2@$_{mono}$ZIF-8 (etching depth indicated at foot of graphic). Peak energies calculated as an average over the 10 spectra.

The O(1s) etched levels revealed a peak at 530.6 eV, characteristic of lattice oxygen in SnO_2 (Figure S6c).[5] Individual spectra of the remaining elements of interest (Figure S6a, S6b and S6d for Zn, N and C spectra, respectively) as well as survey spectra (Figure S7) showed similar homogeneity and consistent peak distribution throughout the etched areas of the composite. The O(1s) spectra (Figure S6c) revealed a higher percentage of oxygen at the unetched MOF surface than at the subsequently etched levels. This is attributed to oxygen adsorption at the composite surface, with a binding energy of 531.8 eV.[6,7] Asymmetric broadening in the O(1s) spectra represents oxygen physically adsorbed to the SnO_2-NPs.[8]

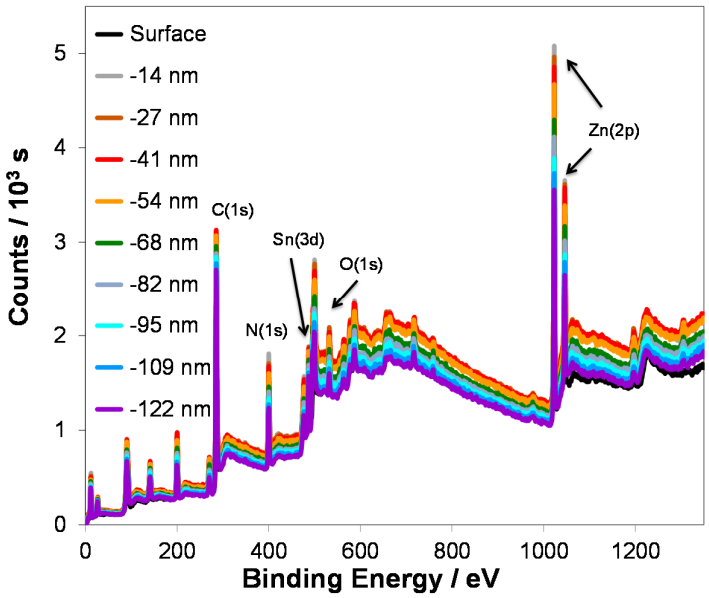

Figure S7. FIB-XPS survey spectra for etched layers of $SnO_2@_{mono}$ZIF-8 (etching depth indicated on left).

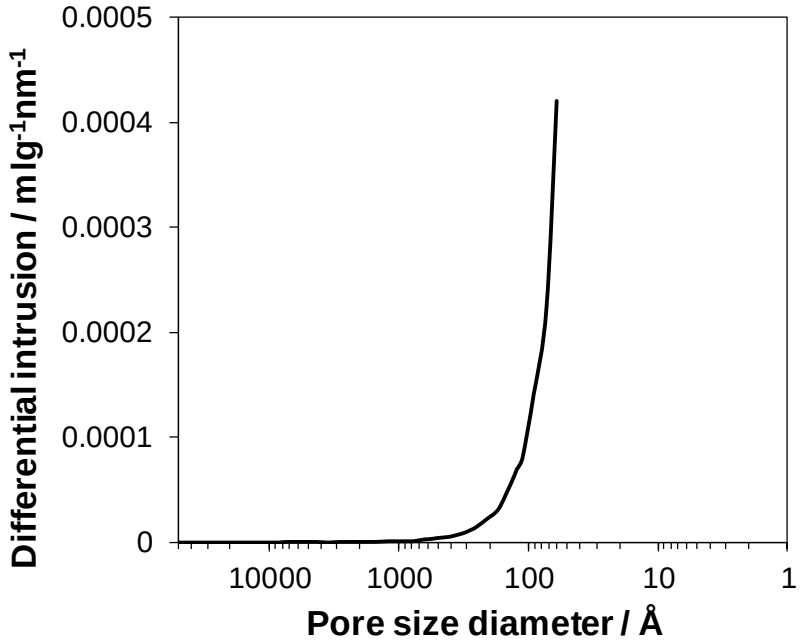

Figure S8: Pore size distribution of the meso- and macroporosity of $SnO_2@_{mono}$ZIF-8 as determined by mercury porosimetry. Note the negligible intruded volumes.

Inspection of the cavity dimensions of pure ZIF-8 (11.6 Å) indicates that the nanoparticles do not reside in the MOF pores, which are too small to accommodate them. Instead, the nanoparticles are encapsulated by the grown ZIF-8 matrix.

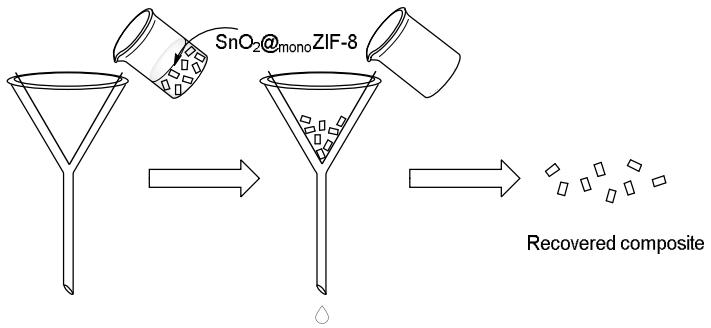

Figure S9. Schematic representation of sample recovery by gravimetric filtration.

Control experiments for the photocatalytic degradation of MB were performed: (i) without solar irradiation in the presence of composite ($SnO_2@_{mono}$ZIF-8) and (ii) with solar irradiation in the absence of composite (Figure S10). A final control experiment, (iii), was conducted to assess the photocatalytic properties of $_{mono}$ZIF-8. Low loading and high loading experiments were performed using 0.4 and 1.7 g of composite or $_{mono}$ZIF-8, respectively. The recyclability was demonstrated by reassessing catalytic activity with fresh dye solution for nine further cycles. Each cycle under solar irradiation was performed parallel to control (i), administering the same gravity filtration recycling procedure in each case (Figure S9).

Error is the standard deviation in triplicated values. Apparent degradation in the absence of simulated solar irradiation is attributed to adsorption of MB to the external surface of the monolith. A number of MOFs are known to have photocatalytic properties of their own,[9,10] with the partial degradation of MB under nanoparticulate ZIF-8 previously attributed to the wide band gap of the semiconducting material. This was explained by the proposed ligand-to-metal-charge-transfer (LMCT) of a 2p HOMO electron from the nitrogen linker into the empty zinc LUMO orbital under stimulation from a UV source.[11,12] For these reasons it was essential to establish whether $_{mono}$ZIF-8 represented a source of potential dye degradation in the current work. Triplicated control experiment (iii) revealed that $_{mono}$ZIF-8 presents no photocatalytic behavior under simulated solar irradiation, with measured dye degradation attributable to surface physisorption (Figure S10). This is consistent with literature solid-state

UV-Vis data for powdered ZIF-8, which suggests that a large band gap of 4.9 eV prevents exciton formation under solar irradiation.[13] However, inspection of the valence and conduction band potentials of SnO_2 reveals that they are positioned such that production of hydroxyl and superoxide radicals, the key species responsible for dye degradation,[14,15] is thermodynamically viable.[16]

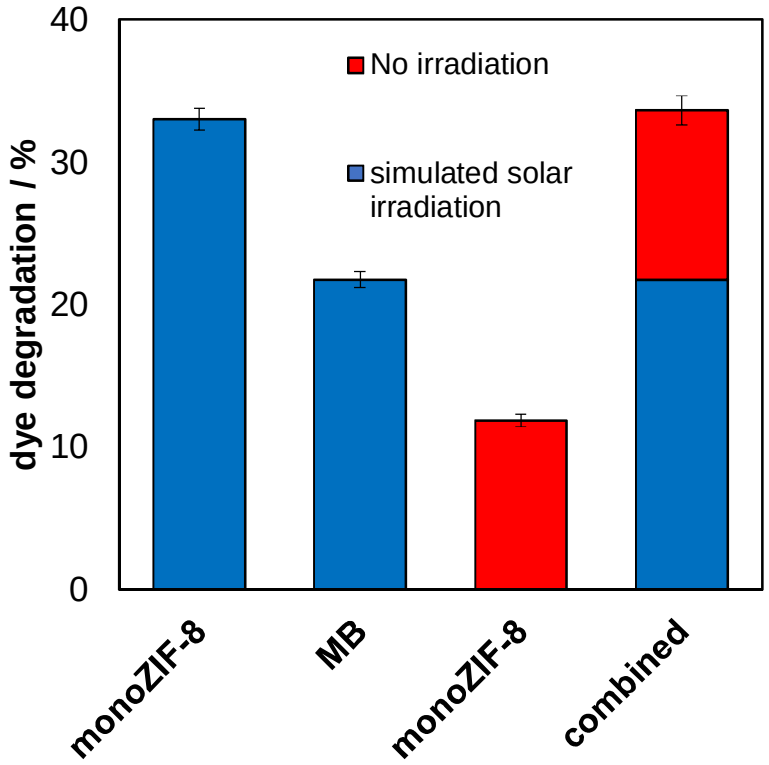

Figure S10. Degradation of MB in the presence of 0.4 g of $_{mono}$ZIF-8 in the presence and absence of solar irradiation. Error bars are the standard deviation in triplicated readings.

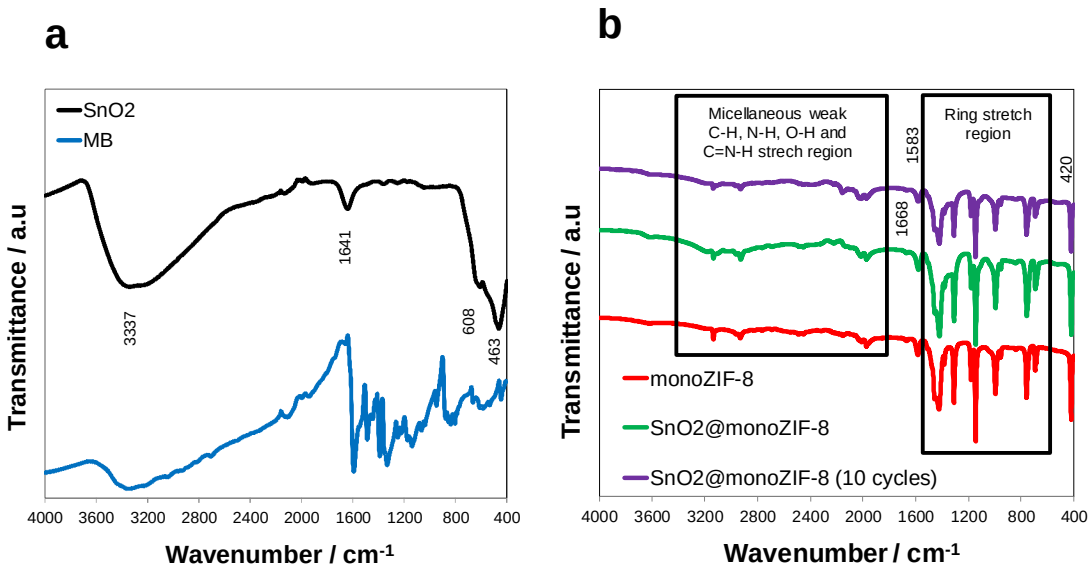

Figure S11. FT-IR spectra of SnO_2 nanoparticles and MB (a) and $_{mono}$ZIF-8, fresh SnO_2@$_{mono}$ZIF-8 and SnO_2@$_{mono}$ZIF-8 after 10 catalytic cycles of MB dye degradation (b).

Dye adsorption is thought to occur predominantly via physisorption to the external surface of the monoliths rather than via chemisorption or coordination to zinc clusters.[6,17] Spectra for SnO_2, $_{mono}$ZIF-8, fresh SnO_2@$_{mono}$ZIF-8 and SnO_2@$_{mono}$ZIF-8 after 10 catalytic cycles were recorded in the range of 400-4000 cm^{-1} (Figure S11). Whilst SnO_2 displays peaks at 1641 and 3337 cm^{-1} corresponding to bending and stretching modes of adsorbed water,[18,19] respectively, the characteristic peaks of the stretching vibrations of Sn-O at 463 and 608 cm^{-1} are not visible in the SnO_2@$_{mono}$ZIF-8 spectrum.[20,21] This is attributed to the relatively low loading of the nanoparticles. Importantly, the key peaks associated with the bending (1668 cm^{-1}) and stretching (1583 cm^{-1}) vibrations of N-H[22] as well as the Zn-N stretching vibration[23] (420 cm^{-1}) and ring stretch region[24] (550-1500 cm^{-1}) in SnO_2@ZIF-8 do not differ in magnitude or frequency on going from the fresh to the cycled composite, suggesting no disruption of the composite bonding regime after exposure to MB dye. Furthermore, no evidence of a NH-O peak[25] (3370 cm^{-1}), Zn-O peak[6] (478 cm^{-1}) is observed in the spectrum of the cycled composite. These would be expected to be seen if the composite was exhibiting chemisorption to the degradation products of MB[26] and this is consistent with there being no chemisorption of dye to the monolith surface.

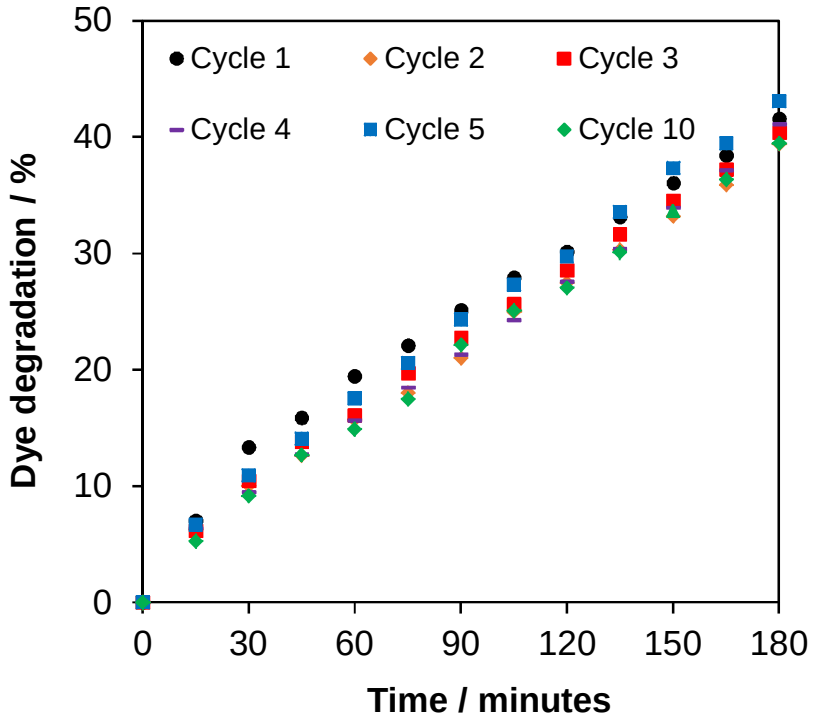

Figure S12. Degradation of MB in the presence of 0.4 g of SnO_2@$_{mono}$ZIF-8 under simulated solar irradiation. All readings are triplicated. Error bars omited for clarity.

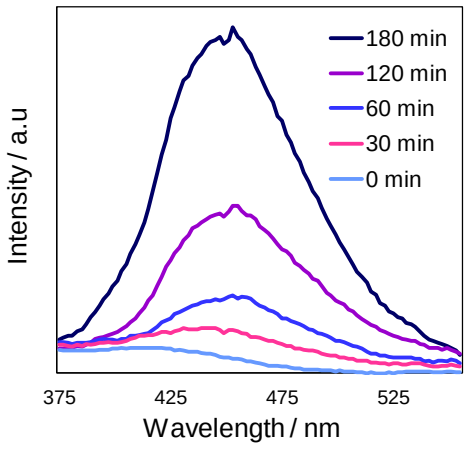

Figure S13. Fluorescence spectral changes measured under simulated solar illumination of 0.4 g of SnO_2@$_{mono}$ZIF-8 in a basic solution of TA (excitation at 315 nm).

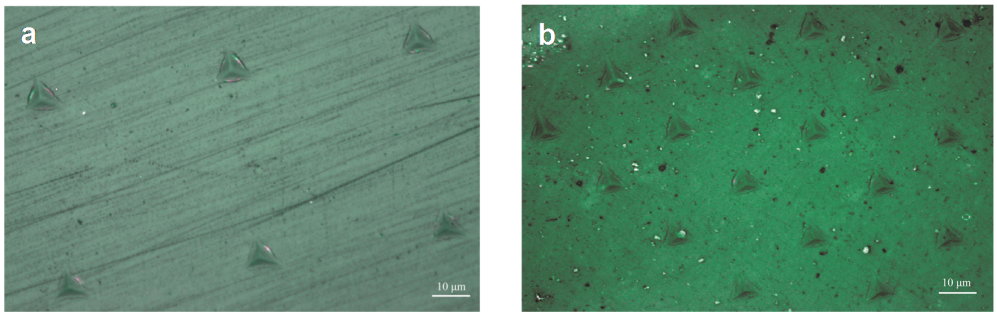

Figure S14. Optical microscopy images of the 3-faced pyramidal indents resulting from 2000 nm depth nanoindentation experiments. (a) $_{mono}$ZIF-8 monolith, (b) SnO_2@$_{mono}$ZIF-8 composite. (Scale bar 10 µm.).

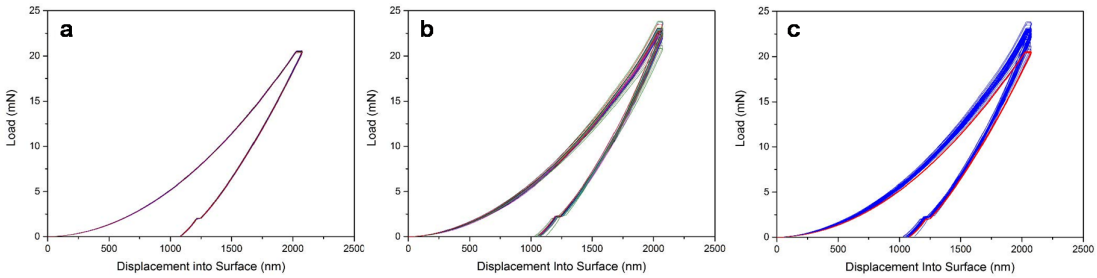

Figure S15. Load-displacement (*P-h*) nanoindentation data for a surface penetration depth of 2000 nm. (a) ZIF-8 monolith on which 9 indentation tests were performed, where highly reproducible *P-h* data reflect the homogeneous nature of the sample tested. (b) SnO_2@$_{mono}$ZIF-8 composite showed a larger scatter in *P-h* data, therefore 48 indents were performed to better establish the sample variability. Combined *P-h* nanoindentation curves (c) in which the red curve depicts the consistent data for $_{mono}$ZIF-8, adjacent to the relatively more varied mechanical response of the SnO_2@$_{mono}$ZIF-8 composite (blue).

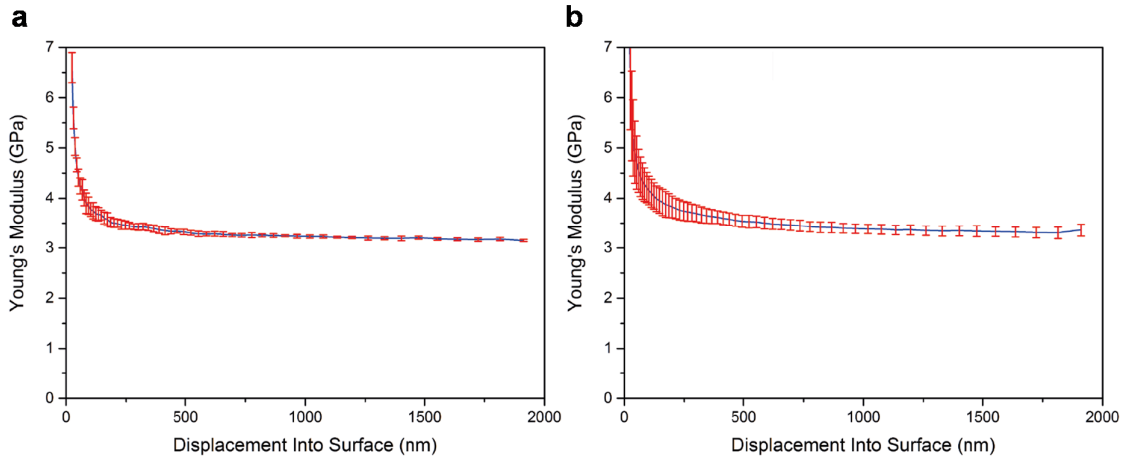

Figure S16. Young's modulus, *E*, of $_{mono}$ZIF-8 (a) and SnO_2@$_{mono}$ZIF-8 (b) plotted as a function of surface penetration depth, where each red error bar corresponds to the standard deviation in 9 and 48 indents, respectively. Averaged Young's moduli of $_{mono}$ZIF-8 and the composite were determined using data collected over the 500-2000 nm indent range, yielding 3.0 ± 0.1 GPa and 3.3 ± 0.1 GPa, respectively.

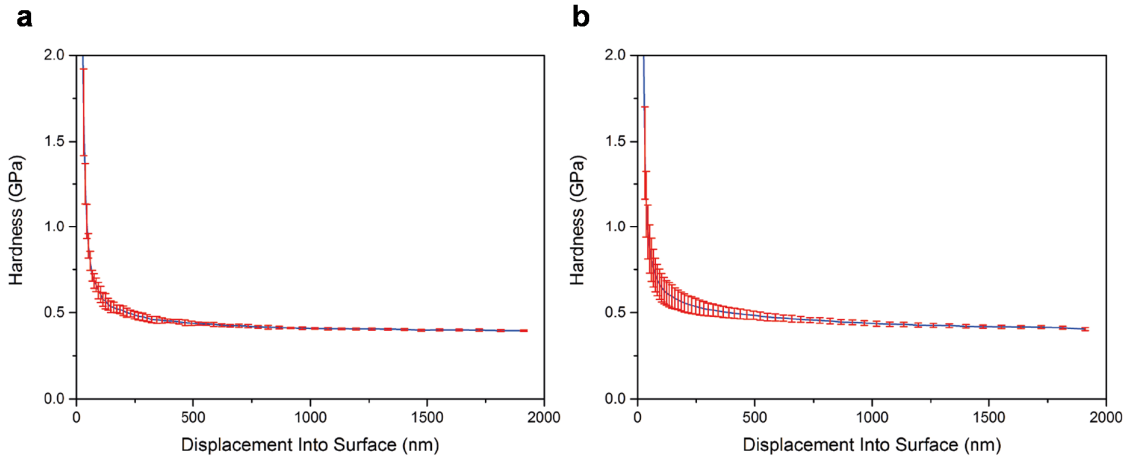

Figure S17. Hardness of $_{mono}$ZIF-8 (a) and SnO_2@$_{mono}$ZIF-8 (b) plotted as a function of surface penetration depth. Each red error bar arises from the standard deviation in 9 and 48 indents, respectively. Averaged hardnesses of $_{mono}$ZIF-8 and the composite were determined using data collected over the 500-2000 nm indent range, yielding 0.41 ± 0.01 GPa and 0.44 ± 0.01 GPa, respectively.

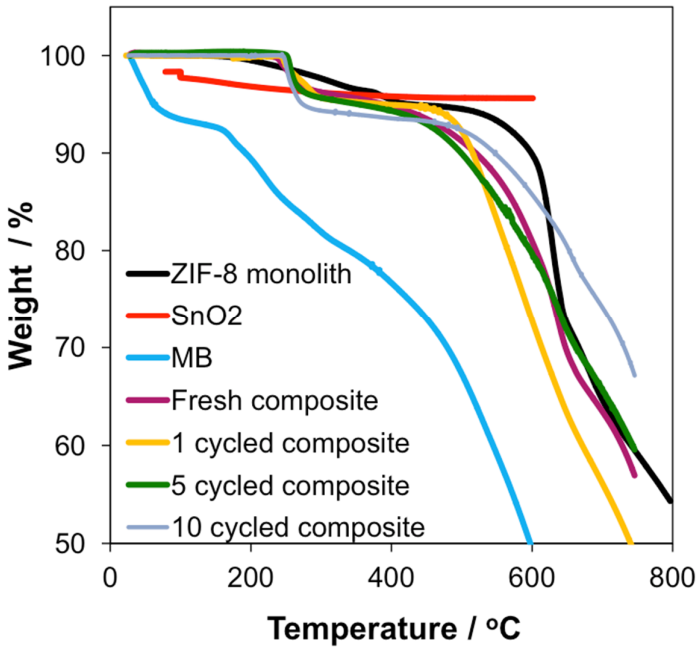

Figure S18. Thermogravimetric analysis of $_{mono}$ZIF-8, SnO_2 NPs, methylene blue (MB), and SnO_2@$_{mono}$ZIF-8 after 0, 1, 5 and 10 catalytic cycles.

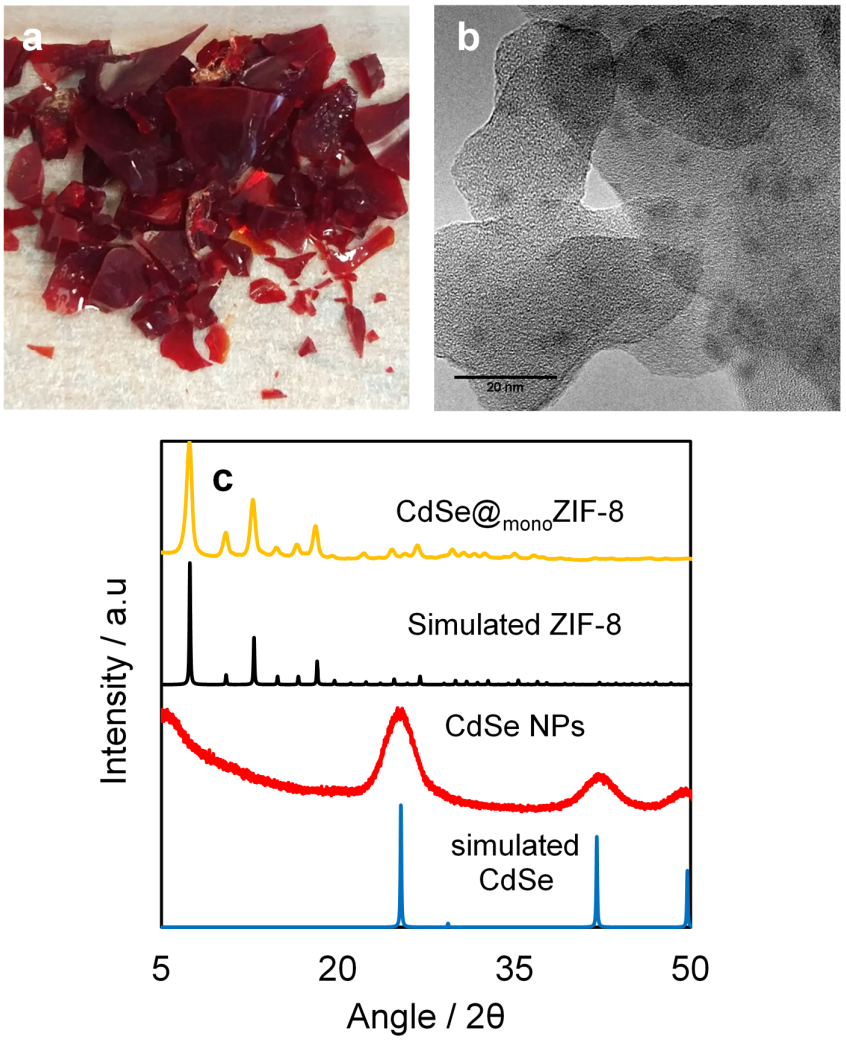

Figure S19. Optical picture (a), TEM micrograhs (b) and PXRD pattern (c) of CdSe@$_{mono}$ZIF-8.

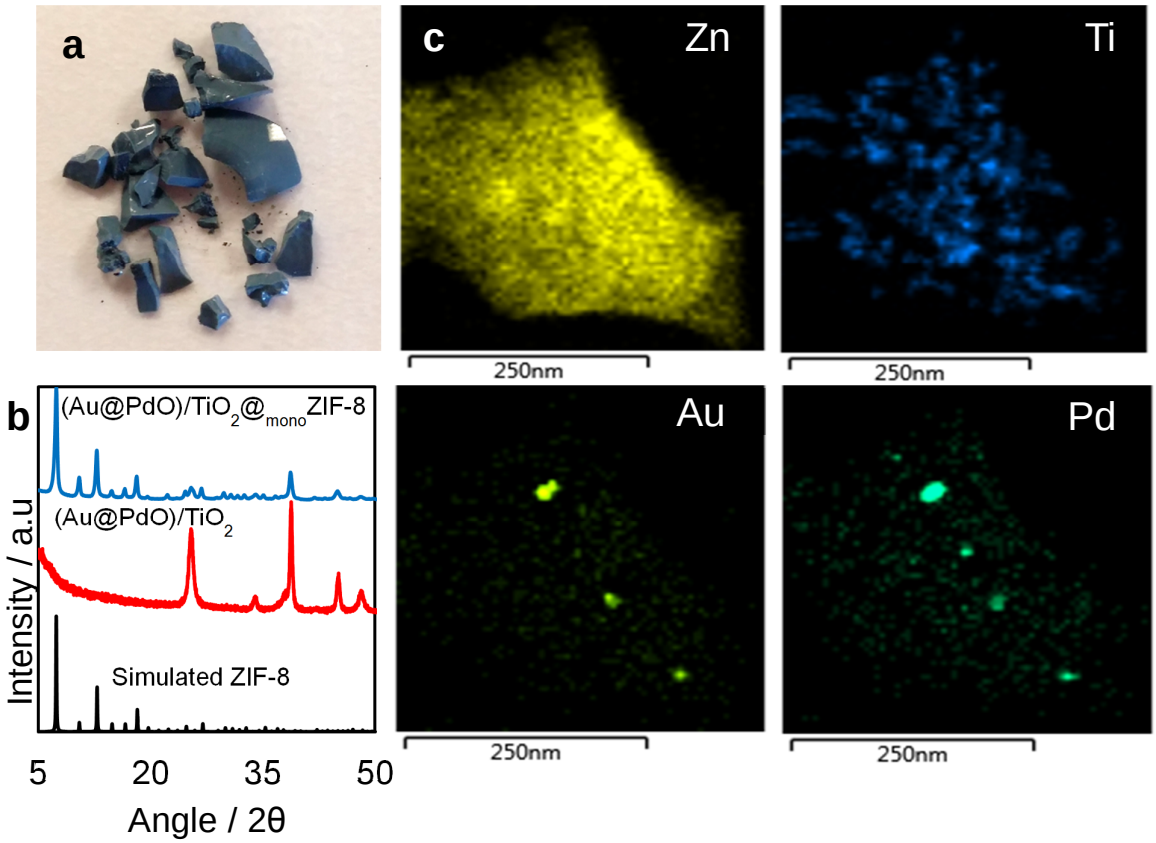

Figure S20. Optical micrograph (a) PXRD trace (b) and STEM-HAADF EDX elemental mapping (c) of (Au@PdO)/TiO_2@$_{mono}$ZIF-8.

4. References

[1] J. Tan, T. D. Bennett, A. K. Cheetham, *Proc. Natl. Acad. Sci. U. S. A.* **2010**, *107*, 9938.

[2] J. C. Tan, B. Civalleri, C. C. Lin, L. Valenzano, R. Galvelis, P. F. Chen, T. D. Bennett, C. Mellot-Draznieks, C. M. Zicovich-Wilson, A. K. Cheetham, *Phys. Rev. Lett.* **2012**, *108*, 1.

[3] X. Xu, J. Zhuang, X. Wang, *J. Am. Chem. Soc.* **2008**, *130*, 12527.

[4] G. . Williamson, W. . Hall, *Acta Metall.* **1953**, *1*, 22.

[5] A. Kar, S. Sain, D. Rossouw, B. R. Knappett, S. K. Pradhan, A. E. H. Wheatley, *Nanoscale* **2016**, *8*, 2727.

[6] M. Jian, B. Liu, G. Zhang, R. Liu, X. Zhang, *Colloids Surfaces A Physicochem. Eng. Asp.* **2015**, *465*, 67.

[7] J.-C. Dupin, D. Gonbeau, P. Vinatier, A. Levasseur, *Phys. Chem. Chem. Phys.* **2000**, *2*, 1319.

[8] L. Cao, H. Wan, L. Huo, S. Xi, *J. Colloid Interface Sci.* **2001**, *244*, 97.

[9] M. Fuentes-Cabrera, D. M. Nicholson, B. G. Sumpter, M. Widom, *J. Chem. Phys.* **2005**, *123*, 124713.

[10] M. A. Nasalevich, M. van der Veen, F. Kapteijn, J. Gascon, *CrystEngComm* **2014**, *16*, 4919.

[11] H.-P. Jing, C.-C. Wang, Y.-W. Zhang, P. Wang, R. Li, *RSC Adv.* **2014**, *4*, 54454.

[12] L. Sun, M. G. Campbell, M. Dinca, *Angew. Chem. Int. Ed.* **2016**, *55*, 3566; *Angew. Chem.* **2016**, *128*, 3628.

[13] F. Wang, Z.-S. Liu, H. Yang, Y.-X. Tan, J. Zhang, *Angew. Chem. Int. Ed.* **2011**, *50*, 450; *Angew. Chem.* **2011**, *123*, 470.

[14] S. Wu, H. Cao, S. Yin, X. Liu, X. Zhang, *J. Phys. Chem. C* **2009**, *113*, 17893.

[15] B. Esen, T. Yumak, A. Sinağ, T. Yildiz, *Photochem. Photobiol.* **2011**, *87*, 267.

[16] R. Vinu, G. Madras, *J. Indian Inst. Sci.* **2010**, *90*, 189.

[17] I. B. Vasconcelos, T. G. da Silva, G. C. G. Militão, T. A. Soares, N. M. Rodrigues, M. O. Rodrigues, N. B. da Costa, R. O. Freire, S. A. Junior, *RSC Adv.* **2012**, *2*, 9437.

[18] S. Blessi, M. M. L. Sonia, S. Vijayalakshmi, S. Pauline, *Int. J. Chem Tech Res.* **2014**, *6*, 2153.

[19] Q. Li, X. Yuan, G. Zeng, Shiquan Xi, *Mater. Chem. Phys.* **1997**, *47*, 239.

[20] Y. Wang, L. Tan, L. Wang, *J. Nanomater.* **2011**, *2011*, 1.

[21] J. Zhang, L. Gao, *J. Solid State Chem.* **2004**, *177*, 1425.

[22] Y. Shen, Y. Zhang, Q. Zhang, L. Niu, T. You, A. Ivaska, *Chem Commun* **2005**, 4193.

[23] M. He, J. Yao, Q. Liu, K. Wang, F. Chen, H. Wang, *Microporous Mesoporous Mater.* **2014**, *184*, 55.

[24] Y. Hu, H. Kazemian, S. Rohani, Y. Huang, Y. Song, *Chem. Commun. (Camb).* **2011**, *47*, 12694.

[25] C. H. Rochester, G. H. Yong, *J. Chem. Soc., Faraday Trans. 1* **1980**, *76*, 1158.

[26] R. Zuo, G. Du, W. Zhang, L. Liu, Y. Liu, L. Mei, Z. Li, *Adv. Mater. Sci. Eng.* **2014**, *2014*, 1.